Improving tangential resolution with a modified delay-and-sum reconstruction algorithm in photoacoustic and thermoacoustic tomography

Pramanik, Manojit

2014

Improving tangential resolution with a modified delay-and-sum reconstruction algorithm in photoacoustic and thermoacoustic tomography

Manojit Pramanik[1,2]

[1]*Biomedical Imaging Laboratory, Electrical Engineering, Indian Institute of Science, Bangalore 560012, India*
[2]*Biomedical Imaging Laboratory, Division of Bioengineering, School of Chemical and Biomedical Engineering, Nanyang Technological University, Singapore 637457 (manojit@ntu.edu.sg)*

Spatial resolution in photoacoustic and thermoacoustic tomography is ultrasound transducer (detector) bandwidth limited. For a circular scanning geometry the axial (radial) resolution is not affected by the detector aperture, but the tangential (lateral) resolution is highly dependent on the aperture size, and it is also spatially varying (depending on the location relative to the scanning center). Several approaches have been reported to counter this problem by physically attaching a negative acoustic lens in front of the nonfocused transducer or by using virtual point detectors. Here, we have implemented a modified delay-and-sum reconstruction method, which takes into account the large aperture of the detector, leading to more than fivefold improvement in the tangential resolution in photoacoustic (and thermoacoustic) tomography. Three different types of numerical phantoms were used to validate our reconstruction method. It is also shown that we were able to preserve the shape of the reconstructed objects with the modified algorithm.   © 2014 Optical Society of America

OCIS codes: (170.3010) Image reconstruction techniques; (170.6960) Tomography; (170.5120) Photoacoustic imaging.

http://dx.doi.org/10.1364/JOSAA.31.000621

1. INTRODUCTION

Photoacoustic and thermoacoustic tomography (PAT and TAT, respectively) are emerging as a hybrid medical imaging modality combining optics/electromagnetics and ultrasound for various clinical uses, such as breast imaging, brain imaging, molecular imaging, and vasculature imaging in small animals [1–14]. In PAT/TAT a short pulsed laser/microwave source irradiates the tissue. Due to absorption of incident energy by the tissue chromophores (such as melanin, red blood cells, and water), there is a local temperature rise, which in turn produces pressure waves emitted in the form of acoustic waves. A wideband ultrasonic transducer receives the acoustic signal (also known as photoacoustic or thermoacoustic waves) outside the tissue (object) boundary. Reconstruction techniques [15–25] are used to map the initial pressure rise within the tissue from the measured (recorded) acoustic waves. Initial pressure is in turn related to the absorption coefficient of the tissue.

Several scanning geometries and transducer recording positions are possible in PAT/TAT. Typically, in a circular scanning geometry the ultrasound transducer (detector) is rotated around the sample in a full circle, and signals are recorded at many locations. Several reconstruction techniques can be used to map the initial pressure rise inside the target object [15–25]. A simple delay-and-sum method implementing a backprojection algorithm is generally used as we are interested in the structural information instead of quantitative images. For more quantitative image reconstructions, iterative image reconstructions or system matrix-based image reconstructions are also proposed [21–25]. However, in this work we will only discuss the time-domain backprojection implementation. Moreover, time-domain backprojection-based reconstruction is faster than the system matrix-based approach [23]. In the reconstructed images, the spatial resolution plays an important role. Figure 1(a) shows the circular geometry generally used in PAT/TAT and how the radial (axial) and tangential (lateral) resolutions are defined with respect to the scanning configuration. In our study, we will only discuss circular scanning geometry. The main factors that determine the spatial resolutions are the finite bandwidth of the ultrasound detection system and the size of the detector aperture. Theoretically it was shown that both the radial and the tangential resolution are dependent on the detector bandwidth. In addition, the tangential resolution is also dependent on the detector aperture size [26]. Bandwidth dependence of spatial resolution is space invariant for any recording geometry, but the aperture dependence of tangential resolution is not space invariant [26]. The tangential resolution is worse near the detector surface compared to locations near the scanning center. This resolution degradation is also referred to as blurring in many places. Blurring that occurs due to the detector's limited bandwidth (typically used for PAT/TAT systems) can be removed by a deconvolution technique if the bandwidth of the detector is known beforehand or at least if it can be measured [27]. However, such a technique cannot improve the tangential
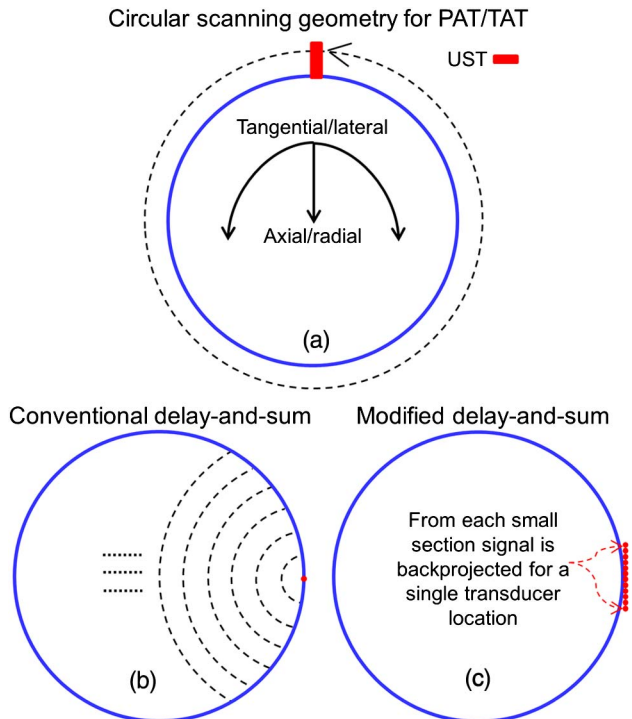
Fig. 1. (a) Circular scanning geometry typically used for PAT/TAT. UST, ultrasonic transducer (detector). Also shows how axial (radial) and tangential (lateral) resolution is defined for this scanning geometry. (b) Conventional delay-and-sum algorithm. (c) Modified delay-and-sum algorithm used in this study. Both are shown for only one transducer signal acquisition location.

resolution degradation caused by the large aperture size of the detector.

If point detectors (or small-aperture detectors) are used in place of large-aperture detectors, they can receive signals from a large angle of acceptance. However, high thermal noise in small-active-area detectors leads to weaker sensitivity. Thus, most practical PAT/TAT systems use large-active-area detectors [8,11,12,15], leading to spatially varying tangential resolution in the reconstructed images. Another way to overcome such problems is to keep the imaging region of interest (ROI) far away from the large detectors surface, leading to a very large scanning radius for the detectors even for a small ROI. This may lead to a space constraint as well as poor signal-to-noise ratio (SNR). Experimentally, it has been demonstrated that use of a negative cylindrical lens [28–31] or high-numerical-aperture-based virtual point detectors [32,33] increases the acceptance angle and improves the tangential resolution in PAT/TAT. However, there are a few practical challenges in such an approach. First, the lens affects the sensitivity of the detector, depending on what material is used to make the lens. Second, when the lens is placed on the transducer surface, air gaps may form between the transducer surface and the lens (generally this happens when the lenses are made in-house in the laboratory instead of during the transducer manufacturing process), which lead to artifacts in the reconstructed images [29]. Third, detectors with an inbuilt lens can also be manufactured, but with a slightly higher cost. Typically the nonfocused ultrasound transducer is cheaper than the focused transducers. Here, we have implemented a modified delay-and-sum reconstruction method, which will improve the tangential resolution of the reconstructed images near the detector surface without using any external lens and without increasing the scanning radius. As a result, normal large-area unfocused detectors can be used for PAT/TAT setup, and with the help of this modified reconstruction algorithm the effect of the aperture on spatial resolution can be minimized.

Numerical phantom simulated data was used to show the efficacy of the modified reconstruction method. We quantified the tangential resolution improvement at various distances from the scanning center with two different sizes of the detectors (typically used in PAT/TAT setup). We also showed that the modified reconstruction algorithm helps to preserve the shape of the target object in the reconstructed images. Moreover, the modified reconstruction works for various numbers of detector positions used for the data collection.

2. METHODS

The initial pressure rise at a position $\vec{r}$ due to a delta light/microwave illumination $\delta(t)$ is given by $p_0(\vec{r}) = \Gamma(\vec{r})A(\vec{r})$, where $A(\vec{r})$ is the spatial light/microwave absorption function, and $\Gamma(\vec{r})$ is the Gruneisen parameter of the tissue. The acoustic pressure $p(\vec{r}_0, t)$ at position $\vec{r}_0$ and time t, initiated by source $p_0(\vec{r})$, satisfies the following photoacoustic wave equation in an acoustically homogeneous medium:

$$\nabla^2 p(\vec{r}_0, t) - \frac{1}{c^2}\frac{\partial^2}{\partial t^2} p(\vec{r}_0, t) = -p_0(\vec{r})\frac{\partial \delta(t)}{\partial t}, \qquad (1)$$

where c is the speed of sound.

The objective of image reconstruction in PAT/TAT is to estimate the initial pressure rise $p_0(\vec{r})$ of the tissue from a set of measured acoustic signals $p(\vec{r}_0, t)$. The exact reconstruction formulas for planar and cylindrical geometry have been derived in the frequency domain [17,18]. However, they may involve multiple integrations or series summations and are complicated to implement. Therefore, an approximate modified backprojection algorithm in the time domain has been deployed to simplify the solution [16,19]. The initial pressure rise can be obtained in the time domain by means of backprojection as follows [19]:

$$p_0(\vec{r}) = \int_{\Omega_0} b\left(\vec{r}_0, t = \frac{|\vec{r} - \vec{r}_0|}{c}\right) \frac{d\Omega_0}{\Omega_0}, \qquad (2)$$

where Ω_0 is the solid angle subtended by the entire measurement surface S_0 with respect to the reconstruction point $\vec{r}$ inside S_0. For planar geometry $\Omega_0 = 2\pi$, and $\Omega_0 = 4\pi$ for spherical and cylindrical geometries. $b(\vec{r}_0, t)$ is the backprojection term; $d\Omega_0$ is the solid angle subtended by detection element dS_0 with respect to reconstruction point at $\vec{r}$. The term $d\Omega_0/\Omega_0$ is a factor weighting the contribution to the reconstruction from the detection element dS_0 (please refer to Figs. 1 and 2 of [19]).

The backprojection term $b(\vec{r}_0, t)$ is given as

$$b(\vec{r}_0, t) = 2p(\vec{r}_0, t) - 2ct\frac{\partial p(\vec{r}_0, t)}{\partial t}. \qquad (3)$$

The reconstruction simply projects $b(\vec{r}_0, t)$ backward via a spherical surface [in our case a circular arc, as our geometry
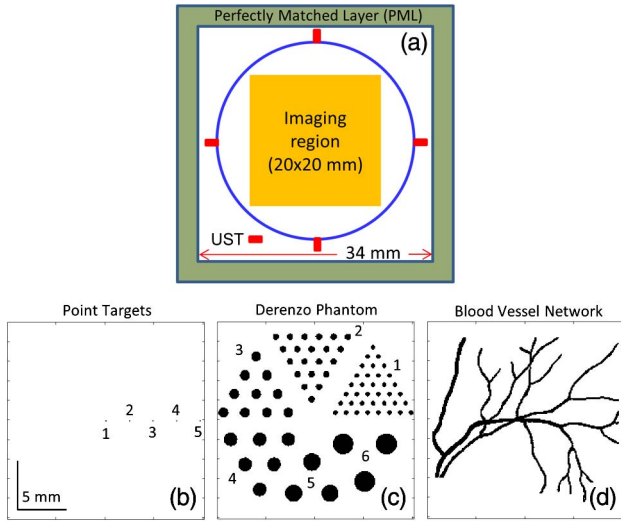
Fig. 2. (a) Schematic diagram of the simulation geometry used. UST, ultrasound transducers (detectors). (b) Point targets phantom, consisting of five point targets (numbered 1–5). (c) Modified Derenzo phantom. (d) Blood vessel network phantom. Initial pressure rises on the targets (black) are 1 and outside are 0.
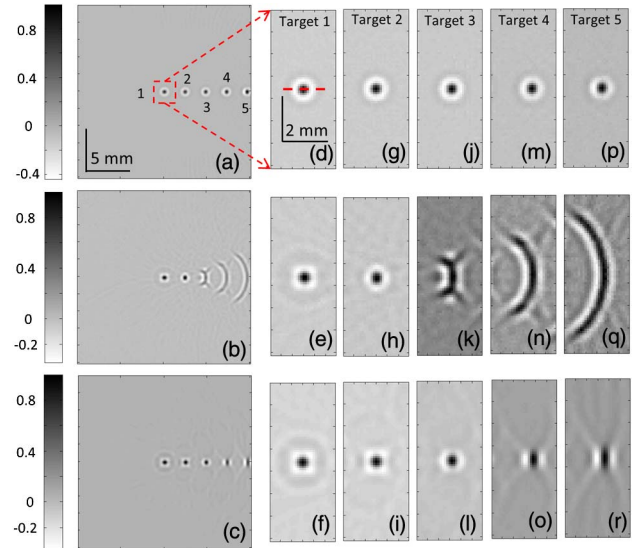

Fig. 3. (a)–(c) Reconstructed point targets with ideal point detector, 12 mm diameter active area detector with conventional reconstruction method, and 12 mm detector with modified reconstruction method, respectively. 200 detector positions are considered for all the reconstructions. Images are normalized. Corresponding color bars are shown. (d)–(r) Zoomed reconstructed images for the point targets: (d)–(f) target 1, (g)–(i) target 2, (j)–(l) target 3, (m)–(o) target 4, and (p)–(r) target 5. All images are normalized in the zoomed region.

is in two dimensions (2D)] centered at position $\vec{r}_0$. A simple delay-and-sum algorithm is typically used to implement this backprojection formula with the recorded pressure wave as the backprojection term, that is, $b(\vec{r}_0, t) = p(\vec{r}_0, t)$. Although in practical PAT/TAT systems, instead of point detectors, large-active-area transducers are used, during reconstruction they are considered as a point detector. Data collected from several positions around the scanning circle are used, and the above backprojection algorithm is implemented to recover the initial pressure rise inside the target object. Since the data collected from a large-active-area transducer is treated as a point detector, it introduces artifacts in the reconstructed image as well as blurs the image.

Now, if we consider the large-aperture detectors, the pressure signal recorded at position $\vec{r}_0$ can be expressed as a surface integral over the detector aperture:

$$p'(\vec{r}_0, t) = \iint p(\vec{r}_0', t) W(\vec{r}_0') \mathrm{d}^2 \vec{r}_0', \qquad (4)$$

where $W(\vec{r}_0')$ is a weighting factor, which represents the contribution from different elements of the detector surface to the total signal of the detector (please refer to Fig. 3 of [26]). In the case of a small flat-aperture detector it was derived [26] that the extension of the point spread function is primarily along the lateral axis when $p'(\vec{r}_0, t)$ is used for reconstruction instead of $p(\vec{r}_0, t)$. Therefore, the tangential resolution is affected by the detector aperture, whereas axial resolution remains unaffected.

Here, in the modified delay-and-sum method, we have considered the area of the detector. Since the signal recorded in the transducer is $p'(\vec{r}_0, t)$, instead of backprojecting $p'(\vec{r}_0, t)$ from $\vec{r}_0$ during reconstruction, we have backprojected it from the entire surface of the detector; that is, the entire integrating surface used to receive the data was utilized in the modified reconstruction. As the proper signal generation physics is incorporated during the reconstruction process it helps in mitigating the tangential resolution problem. Since our recording

geometry is in 2D, the recording surface of the transducer is a line segment instead of a circular surface. Therefore, during reconstruction we have considered many small segments on the line from which the signal $p'(\vec{r}_0, t)$ is backprojected instead of one single point at the middle of the line. Then the same process is repeated for other transducer positions as well. We have used only the first term of Eq. (3) [$b(\vec{r}_0, t) = p'(\vec{r}_0, t)$] for the backprojection for both the unmodified and modified delay-and-sum. Moreover, since the size of the small segments of the transducer is small, all the elements contribute equally to signal detection. Thus the weighting factor $W(\vec{r}_0)$ is uniform and considered to be unity.

A. Simulation

Numerical phantoms were used to generate the forward data for PAT/TAT using the k-wave [34] tool box. This is a open-source MATLAB toolbox that allow the time-domain simulation of PAT/TAT. The k-wave itself can also be used for time-reveral reconstruction of the photoacoustic data. However, in this work the k-wave is used only to generate the simulated photoacoustic data, as we do not have experimental data at present. A desktop computer with an i7 Intel 64 bit processor and 8 GB RAM was used for all the simulations and reconstructions done in this study.

Figure 2(a) shows the simulation geometry used in the study. For simplicity, we have done all the simulations and the reconstructions in 2D without losing generality. The same philosophy and technique can also be extended into three dimensions as well. A computational grid of 341×341 pixels (0.1 mm/pixel) with a perfectly matched boundary layer to satisfy the boundary condition was used for the generation of the forward data. A circular scanning geometry with 15 mm scanning radius was used. The imaging region is restricted to 201×201 pixels (yellow square of size

~20 mm × 20 mm), such that it completely resides inside the scanning circle. A circular imaging region with smaller diameter than the scanning diameter can also be considered. A detector (red bar) was placed on the scanning circle, and forward data was acquired at 200 locations (100 and 300 detector positions are also used in the last part of the study) on the scanning circle distributed uniformly. Three types of detectors were considered for the study. One is an ideal point detector, and the two others are large-aperture nonfocused ultrasonic transducers (12 and 6 mm active area diameter). The k-wave allows users to specify the center frequency and the bandwidth of the detectors as input parameters. We have taken a 2.25 MHz center frequency with 70% nominal bandwidth detectors. The detector parameters are similar to the ultrasound transducers used in practical PAT/TAT systems [12,29]. For the forward simulation a time step of 50 ns with a total of 400 time steps was used. All simulations assumed a sound speed of 1500 m/s. An acoustically homogeneous medium was considered with no absorption or dispersion of sound. The k-wave generates the acoustic pressure waves at the grid points. Therefore, to simulate the signal received by the large detector, the pressure waves at several grid points (falling on the detector surface, in our case the detector line) are added. In all the cases 1% noise was added with the data, resulting in 40 dB SNR level.

Three numerical phantoms were used for the study. Figures 2(b)–2(d) show the three numerical phantoms used. The first one [Fig. 2(b)] consists of five point targets located at distances of 0, 2.4, 4.8, 7.2, and 9.6 mm from the center of the imaging region. The second phantom [Fig. 2(c)] is a variation of the Derenzo phantom. It consists of small as well as large circular targets distributed over the entire imaging region. The targets are grouped as 1–6 depending on their sizes. The third phantom [Fig. 2(d)] is a numerical blood vessel network phantom. Typically PAT is used for blood vessel imaging owing to the high contrast obtained from the blood compared to the background. Therefore, we included such numerical phantoms in our study. In all the phantoms the targets are binary; that is, outside the targets there is no initial pressure rise.

B. Reconstruction

We have implemented the delay-and-sum backprojection reconstruction algorithm in MATLAB. First the conventional reconstruction was implemented, where the pressure wave recorded by a transducer was treated as if it was recorded at a point (center of the transducer). The algorithm can be summarized as follows. Step 1: backproject $p'(\vec{r}_0, t)$ from the center of the transducer for one transducer location $\vec{r}_0$. Step 2: repeat step 1 for all transducer locations. Figure 1(b) shows the backprojection process, where the recorded signal is projected back on the circular arcs (of varying radius depending on the time of arrival of the signal) from the center of the detector. Similarly, the signals from other recording positions are also projected back, and all the projected values are added coherently at every pixel in the reconstructed image. We call this reconstruction method a delay-and-sum implementation of the time-domain backprojection. In the modified reconstruction algorithm instead of considering the broad detector as an approximate point detector at the center of the detector, we considered the entire area of the detector (in this case a line). The line detector is divided into many small segments,

and for each small segment the backprojection is done as before and then the next detector position is considered. We call this method the modified delay-and-sum implementation. The algorithm can be summarized as follows. Step 1: backproject $p'(\vec{r}_0, t)$ from one small segment of the transducer. Step 2: repeat step 1 for all small segments of transducer at location $\vec{r}_0$. Step 3: repeat step 1 and 2 for all transducer locations.

The performance of the modified reconstruction algorithm in terms of improving the reconstructed image quality is quantitatively evaluated using Pearson correlation (PC). It is defined as

$$PC(x, x_r) = \frac{\text{COV}(x, x_r)}{\sigma(x)\sigma(x_r)}, \qquad (5)$$

where x is the actual initial pressure rise distribution and x_r is the reconstructed initial pressure distribution. Here, σ indicates the standard deviation, and COV is the covariance. PC measures the degree of correlation between the target (original initial pressure distribution) and the reconstructed initial pressure distribution, and it can have values ranging from −1 to 1. The higher the value of PC, the better the reconstruction.

3. RESULTS AND DISCUSSION

All reconstructed images shown here are normalized by the maximum pixel value in each image. Figure 3 shows the conventional reconstructed and modified reconstructed PAT/TAT images for phantom one (point targets). The number of detector position around the scanning circle at which data was collected is 200. Figures 3(a)–3(c) are the reconstructed images if the detector was an ideal point detector, 12 mm diameter active area detector with conventional reconstruction, and 12 mm detector with modified reconstruction, respectively. The phantom consists of five point targets located at varying distances from the center of scanning (0, 2.4, 4.8, 7.2, and 9.6 mm. numbered 1–5). Figure 3(a) is the reconstructed images if we had ideal point detectors (not practically feasible). Since all the detectors considered here are band limited, the reconstructed points are no longer points but blobs (blurred points). The best possible spatial resolution achievable for a 2.25 MHz ultrasound transducer is ~0.3 mm (roughly the half
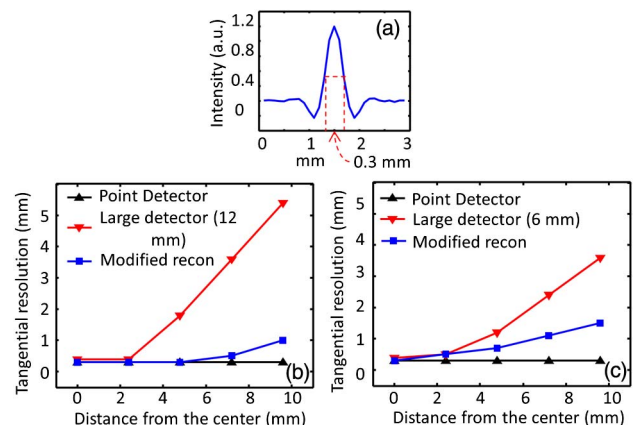

Fig. 4.   (a) Horizontal image profile along the dotted red line [Fig. 3(d)]. Axial resolution at full width at half-maximum is 0.3 mm. (b) and (c) Tangential resolution versus distance from the scanning center for 12 and 6 mm diameter detectors, respectively.

Table 1.   PC of the Reconstructed Initial Pressure Distribution

	Point Targets Phantom		Derenzo Phantom		Blood Vessel Network Phantom	
	6 mm	12 mm	6 mm	12 mm	6 mm	12 mm
Ideal point detector	0.34	0.34	0.66	0.66	0.69	0.69
Large detector with conventional reconstruction	0.19	0.17	0.39	0.31	0.30	0.24
Large detector with modified reconstruction	**0.24**	**0.29**	**0.50**	**0.67**	**0.45**	**0.64**

of the wavelength). With an ideal point detector we were able to achieve that resolution [Fig. 3(a)] of 0.3 mm [full width at half-maximum, shown in Fig. 4(a)] for all the target positions. Figure 3(b) shows that for a practical detector (12 mm diameter active area) if we use conventional reconstruction (where the detector is treated as a point located at the center of the detector), we are unable to reconstruct the points, especially when the point is located far from the scanning center. As we can see, target points 3, 4, and 5 are elongated along the tangential direction; however, in the axial direction there is no elongation. Figure 3(c) shows the same data when used with the modified reconstruction method; we are able to recover the points very close to the ideal reconstruction.

To demonstrate how the target points are reconstructed, we have zoomed the target points from the three reconstructed images as shown in Figs. 3(d)–3(r). The zoomed images were normalized within the zoomed area. It is clearly evident that with modified reconstruction we recovered the target points very close to the ideal ones. We also repeated the simulations with a 6 mm diameter active area transducer. However, for brevity reconstructed images are not shown here. We see a trend similar to the 12 mm detector. The axial resolutions obtained from all the three reconstruction methods are roughly same, in the range of 0.3–0.35 mm for all the target points; however, it is very obvious that the tangential resolution is poor when the target points are far from the scanning center (target points 3–5). Figures 4(b) and 4(c) show the tangential resolution for the target points for all three reconstructions for both the 12 and 6 mm detectors. We see more than five times tangential resolution improvement with the modified reconstruction method for the 12 mm detector and more than two times improvement for 6 mm detector. Also, the larger the detector size, the poorer the tangential resolution for the same distant objects. However, with the modified reconstruction method we were able to recover the points very well even for the farthest point. Table 1 shows the PC values for the reconstructions here. It can be seen that for all the three phantoms (Derenzo and blood vessel phantom data will be presented in the next section), the modified reconstruction method has better reconstruction compared to the traditional method in terms of correlation to the original initial pressure distribution. For both 6 and 12 mm diameter transducers we see significant improvements with our modified algorithm.

Figure 5 shows the results corresponding to the two other types of phantoms; Figs. 5(a)–5(e) are for the Derenzo phantom, and Figs. 5(f)–5(j) are for the blood vessel network phantom. The Derenzo phantom consists of various sized circular objects at various locations. Figure 5(a) [Fig. 5(f) for blood vessel phantom] shows the ideal reconstructed image if the detectors were point detectors. Due to the band-limited nature of the detection we lose low frequency components,

and as a result circular disks are reconstructed as rings. All target groups are reconstructed very well with the ideal point detector. Figures 5(b) and 5(c) [Figs. 5(g) and 5(h) for blood vessel phantom] show the reconstructed images with a 6 mm active area transducer with traditional reconstruction and with modified reconstruction, respectively. Figures 5(d) and 5(e) [Figs. 5(i) and 5(j) for blood vessel phantom] are with the 12 mm detector. Once again we can see with traditional reconstruction [Figs. 5(b) and 5(d)], the objects which are far from the scanning center were not reconstructed properly, whereas with the modified reconstruction we were able to retain the objects' shapes as well as able to clearly obtain the far objects (red arrows). Similar observations were made for blood vessel phantom images in Figs. 5(f)–5(j). With modified reconstruction we are able to delineate the structures better than with traditional reconstruction. The PC values shown in Table 1 also substantiate the improvement in the reconstructed images with the modified reconstruction method.

We repeated the simulations for different numbers of detector positions considered for data collection just to see if that
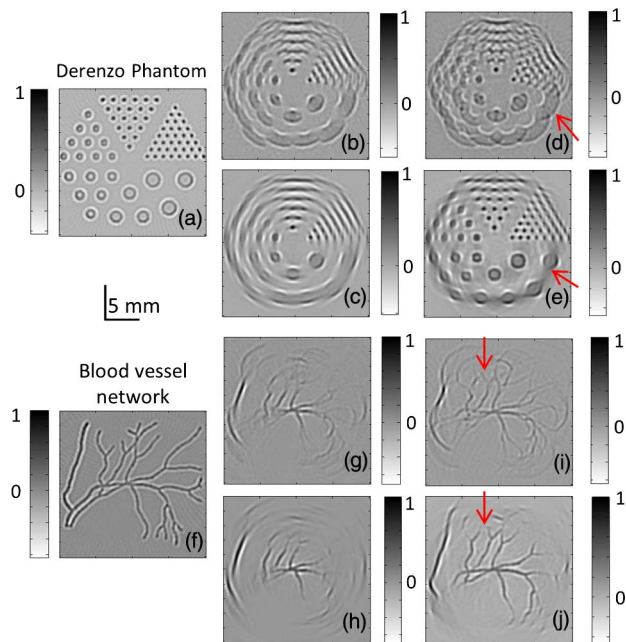

Fig. 5.   (a)–(c) Reconstructed Derenzo phantom with ideal point detector, 6 mm diameter active area detector with conventional reconstruction method, and 6 mm detector with modified reconstruction method, respectively. (d) and (e) are the same as (b) and (c) but with the 12 mm detector. (f)–(h) Reconstructed blood vessel network phantom with ideal point detector, 6 mm detector with conventional reconstruction method, and 6 mm detector with modified reconstruction method, respectively. (i) and (j) are the same as (g) and (h) but with the 12 mm detector. All images are normalized. The color bars are also shown.
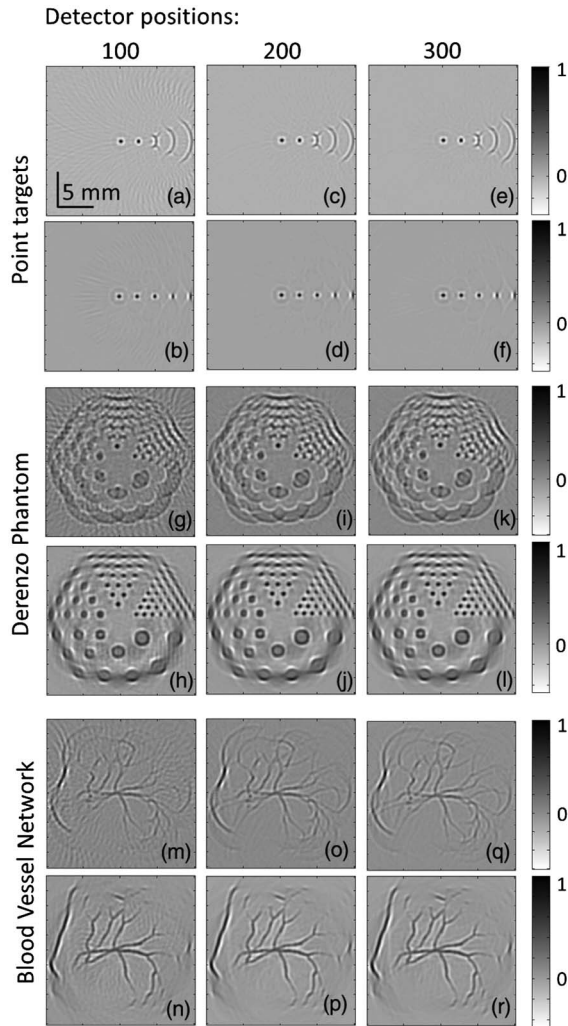
Detector positions:

Fig. 6.   Reconstructed point targets with conventional reconstruction and modified reconstruction methods for 12 mm detector for (a), (b) 100 detector positions, (c), (d) 200 detector positions, and (e), (f) 300 detector positions. (g)–(l) Similar to (a)–(f) with Derenzo phantom. (m)–(r) Similar to (a)–(f) with blood vessel network phantom. All images are normalized. For each row the color bar is shown on the right.
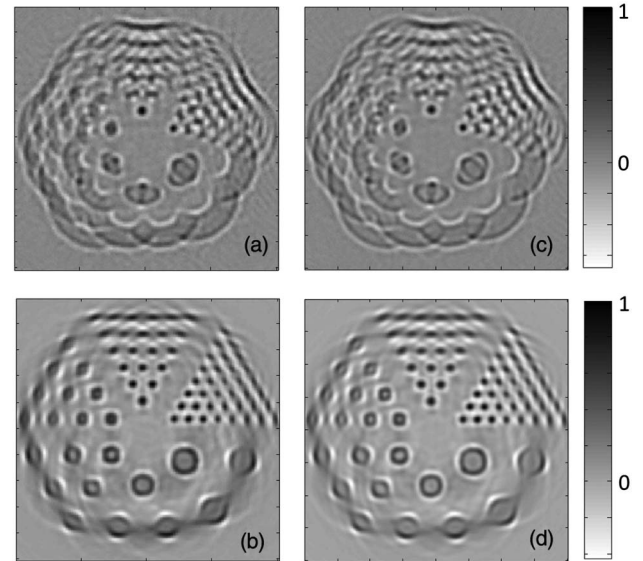

Fig. 7.   Reconstructed Derenzo phantom with conventional reconstruction and modified reconstruction methods for 12 mm detector for (a), (b) 0.1 mm and (c), (d) 0.05 mm pixel size, respectively. All images are normalized. For each row the color bar is shown on the right.

has any effect on our modified reconstruction. Figures 6(a)– 6(r) show the results. We observed that the modified reconstruction algorithm works for different numbers of detector positions as well. Figures 6(a)–6(f) are the reconstructed images for the point target phantom for 100, 200, and 300 detector positions. Only 12 mm diameter detector data is shown here. Figures 6(a), 6(c), and 6(e) are with the conventional reconstruction method, and Figs. 6(b), 6(d), and 6(f) are the corresponding images with the modified reconstruction method. Figures 6(h)–6(l) are for the Derenzo phantom, and Figs. 6(m)–6(r) are for the blood vessel phantom. As expected, we can observe that with the increase of the number of detector positions, the reconstruction artifacts have been reduced.

In the modified delay-and-sum reconstruction algorithm, the broad detector is divided into many small segments for backprojection. At present the number of small segments is automatically decided by the reconstruction program and not directly controlled by the user. The user can only choose

the imaging grid size (in our case the grid size is 0.1 mm/pixel). Then the number of small segments for the transducers is automatically calculated. For example, if the transducer surface is 12 mm, then there will be roughly a total of $12/0.1 = 120$ small segments. So at present to increase the number of segments one has to decrease the grid size (pixel size). We repeated the simulations for a reduced grid size (0–0.05 mm/pixel) for one phantom case just to see if the number of segments has any effect on the reconstructed images. Figures 7(a) and 7(b) are the unmodified and modified delay-and-sum reconstructions for 0.1 mm grid size, respectively. This roughly corresponds 120 small segments for the 12 mm transducer. Figures 7(c) and 7(d) are the unmodified and modified delay-and-sum reconstructions for 0.05 mm grid size, respectively. This roughly corresponds 240 small segments for the 12 mm transducer. As we can see there are hardly any noticeable differences in the reconstructed images. The rule of thumb is that as long as the size of the small segments is less than the resolution of the imaging system, it will be sufficient. In this study the pixel size (0.1 or 0.05 mm) is considerably smaller than the resolution of the imaging system (0.3 mm). Therefore, the number of small segments of the transducer is not affecting the reconstructed images.

We have shown that with a modified reconstruction method one can improve the tangential resolution due to the large aperture of the detectors. The same can also be improved using a negative lens [29]. However, one can avoid the complicated process of lens fabrication, and also attaching the lens on the transducer surface is not an easy step. There is also a loss of signal due to the absorption of ultrasound inside the acrylic lens and another loss due to impedance mismatch between the acoustic coupling medium and the acrylic lens. However, in our approach, since no lens is used, the detector sensitivity remains the same, and as a result we expect higher SNR reconstructed images.

4. CONCLUSION

We demonstrated that by using a modified delay-and-sum time-domain backprojection reconstruction method the tangential resolution can be improved more than fivefold in PAT/TAT. This approach does not need any modification on the transducer; therefore, higher SNR reconstructed images are expected in practice. Three numerical phantoms were used for the demonstration of the resolution improvement. We also showed that the modified reconstruction algorithm preserves the object shape in the reconstructed images, even when the target is far from the scanning center or close to the detector surface. Such shape preservation is important for accurate diagnosis and treatment of tumors.

ACKNOWLEDGMENTS

REFERENCES

1. L. H. V. Wang and S. Hu, "Photoacoustic tomography: *in vivo* imaging from organelles to organs," Science **335**, 1458–1462 (2012).
2. X. D. Wang, Y. J. Pang, G. Ku, X. Y. Xie, G. Stoica, and L. H. V. Wang, "Noninvasive laser-induced photoacoustic tomography for structural and functional *in vivo* imaging of the brain," Nat. Biotechnol. **21**, 803–806 (2003).
3. G. Ku, X. D. Wang, X. Y. Xie, G. Stoica, and L. H. V. Wang, "Imaging of tumor angiogenesis in rat brains *in vivo* by photoacoustic tomography," Appl. Opt. **44**, 770–775 (2005).
4. S. A. Ermilov, T. Khamapirad, A. Conjusteau, M. H. Leonard, R. Lacewell, K. Mehta, T. Miller, and A. A. Oraevsky, "Laser optoacoustic imaging system for detection of breast cancer," J. Biomed. Opt. **14**, 024007 (2009).
5. X. D. Wang, Y. J. Pang, G. Ku, G. Stoica, and L. H. V. Wang, "Three-dimensional laser-induced photoacoustic tomography of mouse brain with the skin and skull intact," Opt. Lett. **28**, 1739–1741 (2003).
6. D. Piras, W. Steenbergen, T. G. van Leeuwen, and S. Manohar, "Photoacoustic imaging of the breast using the Twente photoacoustic mammoscope: present status and future perspectives," IEEE J. Sel. Top. Quantum Electron. **16**, 730–739 (2010).
7. C. H. Li, L. H. V. Wang, A. Aguirre, J. Gamelin, A. Maurudis, and Q. Zhu, "Real-time photoacoustic tomography of cortical hemodynamics in small animals," J. Biomed. Opt. **15**, 010509 (2010).
8. L. H. V. Wang, X. M. Zhao, H. T. Sun, and G. Ku, "Microwave-induced acoustic imaging of biological tissues," Rev. Sci. Instrum. **70**, 3744–3748 (1999).
9. R. A. Kruger, K. K. Kopecky, A. M. Aisen, D. R. Reinecke, G. A. Kruger, and W. L. Kiser, "Thermoacoustic CT with radio waves: a medical imaging paradigm," Radiology **211**, 275–278 (1999).
10. G. Ku and L. H. V. Wang, "Scanning microwave-induced thermoacoustic tomography: signal, resolution, and contrast," Med. Phys. **28**, 4–10 (2001).
11. G. Ku, B. D. Fornage, X. Jin, M. H. Xu, K. K. Hunt, and L. H. V. Wang, "Thermoacoustic and photoacoustic tomography of thick biological tissues toward breast imaging," Technol. Cancer Res. T. **4**, 559–565 (2005).
12. M. Pramanik, G. Ku, C. H. Li, and L. H. V. Wang, "Design and evaluation of a novel breast cancer detection system combining both thermoacoustic (TA) and photoacoustic (PA) tomography," Med. Phys. **35**, 2218–2223 (2008).
13. D. Razansky, S. Kellnberger, and V. Ntziachristos, "Near-field radiofrequency thermoacoustic tomography with impulse excitation," Med. Phys. **37**, 4602–4607 (2010).
14. M. Omar, S. Kellnberger, G. Sergiadis, D. Razansky, and V. Ntziachristos, "Near-field thermoacoustic imaging with transmission line pulsers," Med. Phys. **39**, 4460–4466 (2012).
15. M. H. Xu and L. H. V. Wang, "Pulsed-microwave-induced thermoacoustic tomography: filtered backprojection in a circular measurement configuration," Med. Phys. **29**, 1661–1669 (2002).
16. M. H. Xu and L. H. V. Wang, "Time-domain reconstruction for thermoacoustic tomography in a spherical geometry," IEEE Trans. Med. Imaging **21**, 814–822 (2002).
17. Y. Xu, D. Z. Feng, and L. H. V. Wang, "Exact frequency-domain reconstruction for thermoacoustic tomography. I: planar geometry," IEEE Trans. Med. Imaging **21**, 823–828 (2002).
18. Y. Xu, M. H. Xu, and L. H. V. Wang, "Exact frequency-domain reconstruction for thermoacoustic tomography. II: cylindrical geometry," IEEE Trans. Med. Imaging **21**, 829–833 (2002).
19. M. Xu and L. H. V. Wang, "Universal back-projection algorithm for photoacoustic computed tomography," Phys. Rev. E **71**, 016706 (2005).
20. M. A. Anastasio, J. Zhang, X. Pan, Y. Zou, G. Ku, and L. H. V. Wang, "Half-time image reconstruction in thermoacoustic tomography," IEEE Trans. Med. Imaging **24**, 199–210 (2005).
21. P. Ephrat, L. Keenliside, A. Seabrook, F. S. Prato, and J. J. L. Carson, "Three-dimensional photoacoustic imaging by sparse-array detection and iterative image reconstruction," J. Biomed. Opt. **13**, 054052 (2008).
22. K. Wang, R. Su, A. A. Oraevsky, and M. A. Anastasio, "Investigation of iterative image reconstruction in three-dimensional optoacoustic tomography," Phys. Med. Biol. **57**, 5399–5423 (2012).
23. C. B. Shaw, J. Prakash, M. Pramanik, and P. K. Yalavarthy, "LSQR-based decomposition provides an efficient way of computing optimal regularization parameter in photoacoustic tomography," J. Biomed. Opt. **18**, 080501 (2013).
24. C. Huang, K. Wang, L. Nie, L. H. V. Wang, and M. A. Anastasio, "Full-wave iterative image reconstruction in photoacoustic tomography with acoustically inhomogeneous media," IEEE Trans. Med. Imaging **32**, 1097–1110 (2013).
25. J. Prakash, A. S. Raju, C. B. Shaw, M. Pramanik, and P. K. Yalavarthy, "Quantitative photoacoustic tomography with model-resolution based basis pursuit deconvolution," Biomed. Opt. Express (submitted).
26. M. H. Xu and L. H. V. Wang, "Analytic explanation of spatial resolution related to bandwidth and detector aperture size in thermoacoustic or photoacoustic reconstruction," Phys. Rev. E **67**, 056605 (2003).
27. N. A. Rejesh, H. Pullagurla, and M. Pramanik, "Deconvolution based deblurring of reconstructed images in photoacoustic/thermoacoustic tomography," J. Opt. Soc. Am. A **30**, 1994–2001 (2013).
28. C. H. Li, G. Ku, and L. H. V. Wang, "Negative lens concept for photoacoustic tomography," Phys. Rev. E **78**, 021901 (2008).
29. M. Pramanik, G. Ku, and L. H. V. Wang, "Tangential resolution improvement in thermoacoustic and photoacoustic tomography using a negative acoustic lens," J. Biomed. Opt. **14**, 024028 (2009).
30. W. Xia, D. Piras, J. C. G. van Hespen, W. Steenbergen, and S. Manohar, "A new acoustic lens material for large area detectors in photoacoustic breast tomography," Photoacoustics **1**, 9–18 (2013).
31. W. Xia, D. Piras, M. K. A. Singh, J. C. G. van Hespen, T. G. van Leeuwen, W. Steenbergen, and S. Manohar, "Design and evaluation of a laboratory prototype system for 3D photoacoustic full breast tomography," Biomed. Opt. Express **4**, 2555–2569 (2013).
32. C. H. Li and L. V. Wang, "High-numerical-aperture-based virtual point detectors for photoacoustic tomography," Appl. Phys. Lett. **93**, 033902 (2008).
33. C. H. Li and L. V. Wang, "Photoacoustic tomography of the mouse cerebral cortex with a high-numerical-aperture-based virtual point detector," J. Biomed. Opt. **14**, 024047 (2009).
34. B. E. Treeby and B. T. Cox, "k-wave: MATLAB toolbox for the simulation and reconstruction of photoacoustic wave-fields," J. Biomed. Opt. **15**, 021314 (2010).